Article:
Korsós, M.B. and Erdélyi, R. (2025) Where do solar storms prefer to originate from: hemispheric and longitudinal patterns in solar cycles 23 and 24. The Astrophysical Journal, 989 (2). 162. ISSN: 0004-637X

https://doi.org/10.3847/1538-4357/adee97

The Astrophysical Journal, 989:162 (9pp), 2025 August 20 https://doi.org/10.3847/1538-4357/adee97

Where Do Solar Storms Prefer to Originate From: Hemispheric and Longitudinal Patterns in Solar Cycles 23 and 24

Marianna B. Korsós[1,2,3] and Robertus Erdélyi[2,3,4]
[1] University of Sheffield, School of Electrical and Electronic Engineering, Amy Johnson Building, Portobello Street, Sheffield, S1 3JD, UK
[2] Department of Astronomy, Eötvös Loránd University, Pázmány Péter sétány 1/A, H-1112 Budapest, Hungary
[3] Gyula Bay Zoltán Solar Observatory (GSO), Hungarian Solar Physics Foundation (HSPF), Petőfi tér 3, H-5700 Gyula, Hungary
[4] Solar Physics and Space Plasma Research Centre, School of Mathematical and Physical Sciences, University of Sheffield, S3 7RH, UK
Received 2025 April 29; revised 2025 July 6; accepted 2025 July 9; published 2025 August 12

Abstract

Using synoptic maps, we analyzed the relationship between active longitudes, the most populated longitudes of energetic flares, the distribution of magnetically complex active regions, and the preferred locations of those that produced the largest flares. We found that solar activity was stronger in the northern hemisphere during the rising phases of both cycles, shifting to the southern hemisphere around solar maximum. In solar cycle 24, stronger activity returned to the northern hemisphere during the declining phase—a pattern not seen in cycle 23. Strong magnetic elements and large flares showed significant clustering along persistent active longitudes, particularly from the solar maximum through the declining phase. These active longitudes remained stable for four to nine Carrington rotations before shifting by approximately 160°–180°, and their evolution displayed clear periodic behavior with cycles ranging from 0.6 to 2.02 yr, consistently seen both in the magnetic and flare data. During the solar minimum between cycles 23 and 24, active longitudes clustered near 200° longitude for about 3 yr, with cycle 24 beginning with a dominant activity at this location. Furthermore, 71% of β–γ–δ-type active regions that produced X-class flares emerged along these active longitudes. This highlights their significance for the strongest solar eruptions and offers valuable potential information for midterm flare prediction in both hemispheric and longitudinal domains, even at the onset of new cycles.

Unified Astronomy Thesaurus concepts: Active Sun (18); Solar active regions (1974)

1. Introduction

Active longitudes are concentrated longitudinal band regions on the Sun where magnetic activity tends to concentrate over time, influencing solar activity patterns. The concept of active longitudes has a long-standing history in solar physics. In 1863, R. C. Carrington (1863) documented that sunspots are not randomly distributed across longitudes but are instead accumulated in distinct longitudinal bands characterized by heightened activity. Over the years, these regions have been studied extensively and were identified across various solar activity indices, leading to their characterization under diverse terminologies, including active longitudes (J. I. Vitinskij 1969), activity sources (V. Bumba & R. Howard 1969), Bartels active longitudes (V. Bumba & R. Howard 1969), streets of activity (W. Stanek 1972), sunspot nests (M. J. M. Castenmiller et al. 1986), hot spots (T. Bai 1990), helicity nests (A. A. Pevtsov & R. C. Canfield 1999), complexes of activity (E. E. Benevolenskaya et al. 1999), etc. to name a few alternatives.

Active longitudes on the Sun leave their imprint on all the outer layers of the solar atmosphere penetrated by magnetic fields. Studies on active longitudes have consistently suggested that various solar activity proxies, including sunspots (H. Balthasar & M. Schüssler 1984; E. E. Benevolenskaya et al. 1999; V. Bumba et al. 2000; S. V. Berdyugina & I. G. Usoskin 2003; D. A. Juckett 2006), the heliospheric magnetic field (A. Ruzmaikin et al. 2001; J. Takalo & K. Mursula 2002; K. Mursula & T. Hiltula 2004), solar faculae (V. P. Mikhailutsa & V. V. Makarova 1994; A. Elek et al. 2024; K. Mursula & T. Hiltula 2004), solar flares and coronal mass ejections (V. Bumba & R. Howard 1969; T. Bai 1988, 2003; L. Y. Zhang et al. 2007; N. Gyenge et al. 2016, 2017), macrospicules (T. S. Kiss et al. 2017; T. S. Kiss & R. Erdélyi 2018), bright points (I. Sattarov et al. 2005; S. W. McIntosh et al. 2017), and coronal off-limb structures (S. Bourgeois et al. 2025) show a pronounced preference for specific longitudinal ranges, thereby reinforcing the idea of the potential presence of active longitude belts and the notion of active longitudes.

Furthermore, several studies have shown that active regions disobeying the hemispheric helicity rule appear to form in "activity nests" or active longitudes (R. C. Canfield & A. A. Pevtsov 1998; A. A. Pevtsov & R. C. Canfield 1999; H. Zhang & S. Bao 1999; A. A. Pevtsov & R. C. Canfield 2000; L. Tian et al. 2001; A. A. Pevtsov & K. S. Balasubramaniam 2003). Helicity in active regions is likely related to the subsurface dynamo processes, and thus, the presence of these helicity nests may suggest their subphotospheric origin. However, J. Pelt et al. (2005, 2006) employed surrogate data, Monte Carlo simulations, and a broad parametric search, concluding that the active longitudes could be a coincidence of random fluctuations rather than a real phenomenon.

Persistent active longitudes, though influenced by differential rotation, remain stable over time; however, the overall active region landscape within them is constantly changing due to intense magnetic flux emergence (V. Gaizauskas et al. 1983). Only a few active regions survive for one or two, and occasionally up to three or four Carrington rotations (CRs; M. A. Weber et al. 2023). While activity decreases at one longitude, it may increase at another, indicating a shift of the spotted area across hemispheres (I. G. Usoskin et al. 2007).

When activity levels are similar across longitudes, dominance switches from one hemisphere to the other. This cycle of sunspot activity alternates between active longitudes approximately every 1–3 yr (S. V. Berdyugina & S. P. Järvinen 2005). Also, S. Mandal et al. (2017) and I. Tähtinen et al. (2024) found ∼1.3–2.2 yr periodic behavior in the evolution of active longitudes. Active longitudes are typically observed to be 20°–60° wide (V. Bumba & R. Howard 1969; T. Bai 1988, 2003; E. V. Ivanov 2007; N. Gyenge et al. 2016) for about 10–15 CRs (A. Elek et al. 2024). D. A. Juckett (2006) found 0.9–5.5 yr oscillations in surface spherical harmonics of sunspot longitudinal distributions.

Nevertheless, the underlying mechanisms driving these spatiotemporal patterns remain the subject of ongoing debate. From a theoretical perspective, current dynamo models have yet to fully account for—or predict—the emergence of active longitudes. Moreover, M. B. Korsós et al. (2024) presented observational evidence suggesting that active longitudes may play a significant role in predicting upcoming solar storm seasons. Building on this, the present work further investigates the relationship between the most populated latitudes and longitudes of strong magnetic field concentrations and energetic flares, the distribution of magnetically complex active regions relative to active longitudes, and the locations of those regions that produced the most powerful flares in comparison to active longitudes. Before starting the data analysis, we first applied a simple synthetic model to explore how the evolution of active longitudes would appear over a solar cycle under the assumption that active longitudes exist with their reported properties.

Therefore, this work is structured as follows: Section 2 discusses how the evolution of the most populated longitude develops from one CR to the next over the course of the solar cycle, under the assumption that active longitudes are either present or absent. Section 3 provides a brief but comprehensive overview of the synoptic data sets and flare catalogs utilized in this study. In Section 3, we also describe the methodologies employed to identify and analyze the evolution of active longitudes throughout solar cycles 23 and 24. This section also includes an analysis of how the most magnetically complex active regions are distributed along the identified active longitudes. Finally, Section 4 summarizes our key findings and suggests directions for future research based on the insights gained from this study.

2. Reconstructing the Pattern of Most Populated/Active Longitude Based on Synthetic Data

To explore how active longitude might evolve over a solar cycle, we first generated 1000 synthetic active regions spanning an 11 yr cycle, reflecting the typical number observed during such a period. The synthetic sunspot data set includes both latitude and longitude coordinates. The latitudinal distribution of the 1000 synthetic active regions is designed to follow the typical solar cycle pattern, with sunspots emerging at higher latitudes early in the cycle and gradually migrating toward the equator. We did not include area or polarity information, as these parameters are not taken into account in the observational analysis either. In this study, we examined two scenarios:

1. The first scenario represents a random distribution of sunspots, without considering the lifespans of active regions across multiple CRs.
2. In contrast, the second scenario simulates persistent populated/active longitudes, where this zone remains active for several rotations—typically between 4 and 10 CRs. The choice of lifetime is based on earlier studies: A. Malik & M. Bohm (2009) identified average lifespans of three to five rotations, while A. Elek et al. (2024) reported durations of 10 to 15 rotations. Although E. V. Ivanov (2007) suggested lifetimes of 15 to 20 rotations, we excluded such long-lived structures from this test, as A. Malik & M. Bohm (2009) found considerably shorter durations to be more common, and the findings of A. Elek et al. (2024) also support a shorter typical range.

For each CR during the simulated cycle, kernel density estimation (KDE) was applied to the longitudinal coordinates of the synthetic active regions using the `SciPy` Python package.[5] KDE is a nonparametric statistical method used to estimate the probability density function of a continuous variable based on observed data (M. Rosenblatt 1956; E. Parzen 1962). This technique is essential for identifying the most populated longitudes in each CR, like in Figure 2.

1. The left panel of Figure 1 illustrates the first scenario, showing scattered KDE peaks with no distinct concentration of active longitudes due to the random and short-lived nature of the simulated regions.
2. The right panel of Figure 1 displays the second scenario, in which long-lived regions produce distinct, persistent concentrations at certain longitudes, resulting in a clearer pattern of evolving active longitudes.

Having established a synthetic reference for how the populated or active longitudes may evolve over a solar cycle, we now turn to the observational data. Specifically, we investigate whether strong magnetic field elements and major flares exhibit similar clustering behavior during solar cycles 23 and 24.

3. Activity Clustering during Solar Cycles 23 and 24

3.1. Data Preparation

In order to achieve our goal, we analyzed the evolution of synoptic maps. A synoptic map is a comprehensive representation of the Sun's surface, constructed by compiling observations over a full solar rotation—approximately 27.2753 days, known as a CR. In this work, we adopted different types of synoptic map data, including those from the photosphere, chromosphere, and flare observations. The descriptions of these maps are:

1. *Solar and Heliospheric Observatory (SOHO) and Solar Dynamics Observatory (SDO) magnetic synoptic maps*. For solar cycles 23 and 24, we employed the SOHO/Michelson Doppler Imager (MDI) synoptic maps[6] and SDO/Helioseismic and Magnetic Imager (HMI) synoptic maps [7] for our analyses. SOHO/MDI (P. H. Scherrer

[5] https://www.scipy.org/citing-scipy/
[6] http://soi.stanford.edu/magnetic/index6.html
[7] http://jsoc.stanford.edu/jsocwiki/SynopticMaps

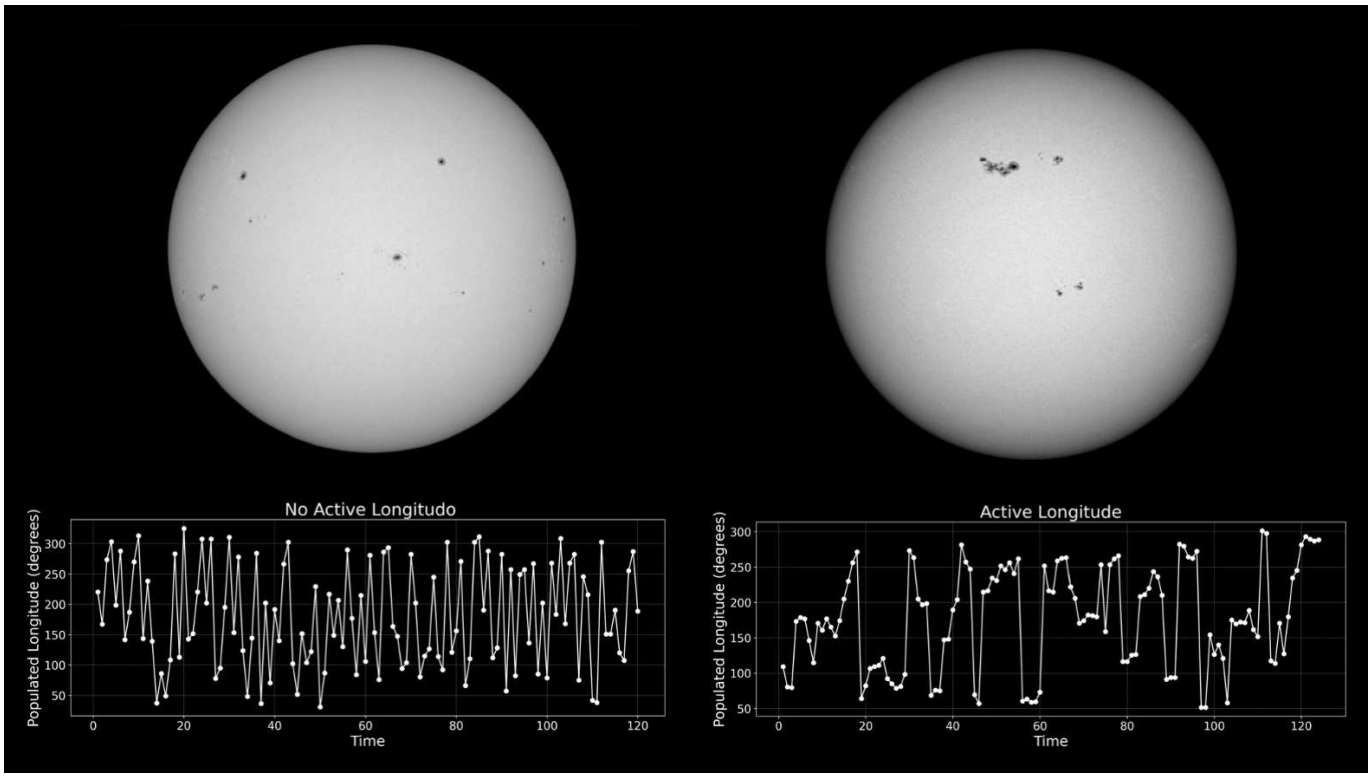

Figure 1. This image demonstrates two simulated cases: "No Active Longitude" (left) and "Active Longitude" (right). The solar images are real observations, used here for illustrative purposes. In the "No Active Longitude" case, sunspots are randomly scattered on the solar disk without clear clustering, resulting in a highly irregular time series plot. In contrast, the "Active Longitude" case shows sunspots clustering at specific longitudes, with a more structured time series pattern, indicating the presence of persistent magnetic structures.

et al. 1995) observed the full solar disk in Nickel (Ni) 6768 Å absorption lines. The SOHO/MDI magnetic synoptic maps are generated from 20 definitive level 1.8 observations. The SOHO/MDI images are recorded on an array of 1024×1024 pixels, and the spatial resolution of a SOHO/MDI magnetogram is $4''$ over the whole solar disk. We adapted the SDO/HMI line-of-sight synoptic maps (Y. Liu et al. 2017), which are based on the photospheric absorption line of iron (Fe I) at 6173.3 Å. The HMI Magnetogram, with a 720 s temporal resolution line of sight, has a pixel resolution of $0.''504$ (P. H. Scherrer et al. 2012; J. Schou et al. 2012). The effective temporal width for contributions to these synoptic maps is approximately three hours. This period involves the acquisition of 20 magnetograms, each lasting 720 s, centered around 90 minutes of central meridian passage. Consequently, the final HMI synoptic maps are composed at a resolution of 3600×1440 pixel^2.

To investigate the evolution of strong magnetic fields in the synoptic maps, we focused on regions where the magnetic field strength exceeded $|\pm 500|$ G. Accordingly, we analyzed the stronger magnetic field components in SOHO/MDI synoptic maps from CR 1909 to 2106. For SDO/HMI data, we incorporated synoptic maps covering CR 2107 to 2209.

2. *SOLIS magnetic synoptic maps*. Also, for solar cycle 24, spanning 2010–2017, we utilize radial magnetic flux synoptic map observations of the solar photosphere and chromosphere with the Fe I 6302 Å and Ca II 8542 Å lines from the vector Stokes magnetograph (VSM) on the Synoptic Optical Long-Term Investigations of the Sun (SOLIS; C. U. Keller et al. 2003; K. S. Balasubramaniam & A. Pevtsov 2011). We use SOLIS/VSM[8] observations alongside SDO/HMI, as solar flares do not occur in the photosphere but rather in the chromosphere or above. It is also important to note that in the chromosphere, the large-scale flux distribution is less constrained compared to the photosphere.

The SOLIS radial magnetic flux synoptic map is the weighted-mean radial flux at each projected-longitude-latitude bin of the given CR. Fluxes are included from all observations overlapping these Carrington longitudes, and are weighted in longitude so that the strongest weight is given to longitudes observed near the central meridian. Additional details about the algorithm for generating the synoptic maps can be found in L. Bertello et al. (2014). The SOLIS synoptic maps are available in two resolutions, 180 by 360 (latitude–longitude) pixel^2 and 900×1800 pixel^2. In this work, we use the 900×1800 pixel^2 maps.

3. *Flare catalog—constructing a synoptic map.* To identify the strong flare activity period(s) of solar cycles 23 and 24, we used the Geostationary Operational Environmental Satellite (GOES)[9] catalog covering the era from 1975. In this catalog, the A/B/C/M and X flare classes are defined based on the near-Earth measurements of the maximum X-ray flux at wavelengths from 1 to 8 Å. M- and X-class flares are the strongest ones.

[8] https://nso.edu/telescopes/nisp/solis/

[9] https://www.ngdc.noaa.gov/stp/space-weather/solar-data/solar-features/solar-flares/x-rays/goes/xrs/

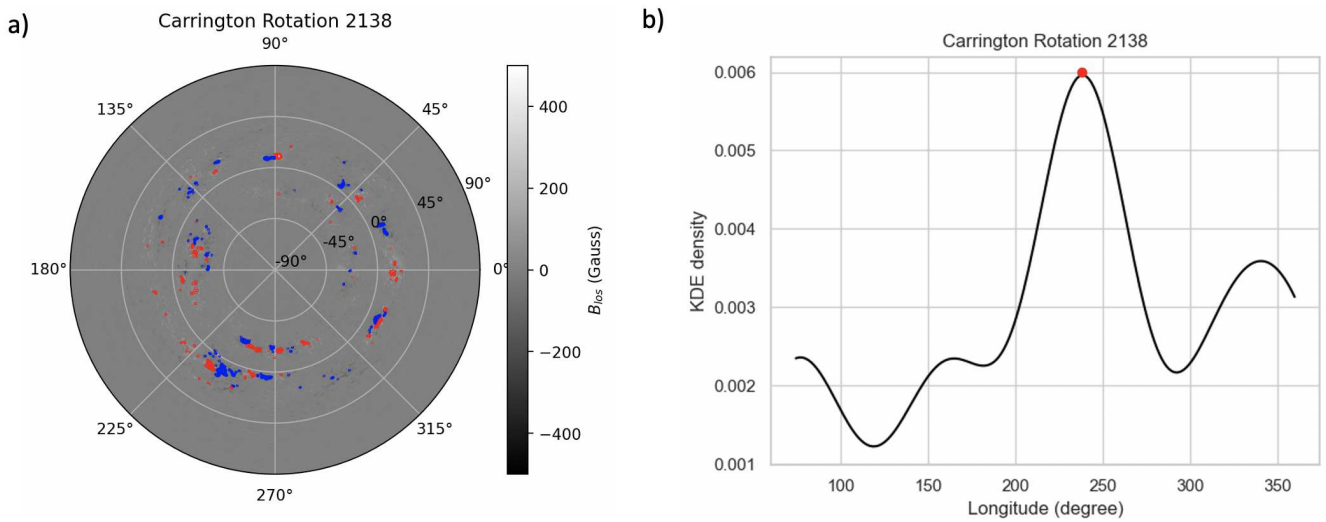

Figure 2. Panel (a) displays a synoptic map associated with CR 2138, derived from photospheric SOLIS observations and presented in a polar coordinate system. This map highlights areas of strong magnetic fields, with red indicating positive fields and blue denoting negative fields, each exceeding |±500| Gauss, respectively. Panel (b) shows the most populated longitude, 238° (indicated by the red dot), of Carrington rotation (CR) 2138, as determined using Kernel Density Estimation (KDE).

In the presented work, only M- and X-class flares were considered for analyzing the periods of intense flare activity within each solar cycle. We constructed synoptic maps for M- and X-class flares based on their coordinates and times as listed in the catalogs. The onset time of each flare was converted into the corresponding CR, which facilitated the calculation of longitudinal positions on the Carrington map. The start and end dates of each CR are documented from 1853 and available online,[10] allowing us to determine which flare corresponds to a given CR. The latitude value of each flare was taken directly from the GOES catalog. This approach enables us to accurately overlay flare locations onto the synoptic maps.

As a next step, to determine whether there is clustering of stronger magnetic field elements and large energetic flares not only longitudinally but also latitudinally, we extracted the Carrington longitude and latitude coordinates of magnetic field elements and flares from synoptic maps. Figure 2(a) shows an example of such a synoptic map—specifically, the photospheric SOLIS synoptic map for CR 2138—displayed in a polar coordinate system. In this map, red indicates positive and blue indicates negative strong magnetic field elements (greater than |±500|G). Subsequently, KDE was applied to the latitudinal and longitudinal coordinates of the magnetic field elements and flares. For illustration, Figure 2(b) shows the KDE result for the longitudinal distribution of magnetic elements during CR 2138. The most populated longitude (i.e., the peak density location) is marked with a red dot at 238°.

The most populated latitudes and longitudes for each CR are plotted in Figure 3 to support further analysis.

3.2. Populated Hemisphere

First, we focus on the evolution of the most populated latitudinal locations identified as the largest peaks in the 1D KDE of strong magnetic field elements and flares during each CR. At first glance, there is clear clustering of these most populated latitudes in both hemispheres throughout each solar cycle. To quantify this clustering, we applied 2D KDE with the results shown as gray contour levels in Figures 3(a)–(b) and Figures 4(a)–(b). These contours provide a smoothed density representation of the scatter plot of 1D KDE peak latitudes over time. The light gray areas only encompass the 1D KDE peaks, which are distributed across solar cycles 23 and 24. The mid-gray contours clearly depict the latitudinal migration of solar activity throughout a solar cycle. Most notably, the darkest gray regions within the butterfly diagram highlight persistent activity concentrations, revealing hemispheric asymmetries as well as differences in the timing and duration of magnetic activity during the solar cycles.

Focusing on the darkest gray areas in panels (a) and (b) of Figure 3, we observe that, for both the strong magnetic field elements and the solar flares, activity was more prominent in the northern hemisphere during the rising phases of solar cycles 23 and 24. During the maximum periods of these cycles, however, the southern hemisphere exhibited greater activity. Notably, during solar cycle 23, the southern hemisphere remained active until the end of the cycle, whereas in solar cycle 24, activity shifted back to the northern hemisphere during the declining phase. This activity trend is visible in Figure 3(a) and becomes even more pronounced when solar cycle 24 is examined separately in Figures 4(a)–(b). Panels a-b depict the SOLIS photospheric and chromospheric synoptic maps, respectively. Figures 4(a)–(b), as previously mentioned, reveal a consistent pattern: magnetic activity was concentrated in the northern hemisphere at the beginning of the cycle, shifted toward the southern hemisphere around solar maximum, and returned to the northern hemisphere during the declining phase.

In contrast, Figure 3(b), which presents the 2D KDE analysis of the flare activity, does not capture this hemispheric evolution as clearly during solar cycle 24. However, the trend could still be visually inferred. Therefore, further analysis is needed to more accurately identify the spatial and temporal

[10] https://www.astroleague.org/files/obsclubs/Carrington%20Rotation%20Start%20Dates.pdf

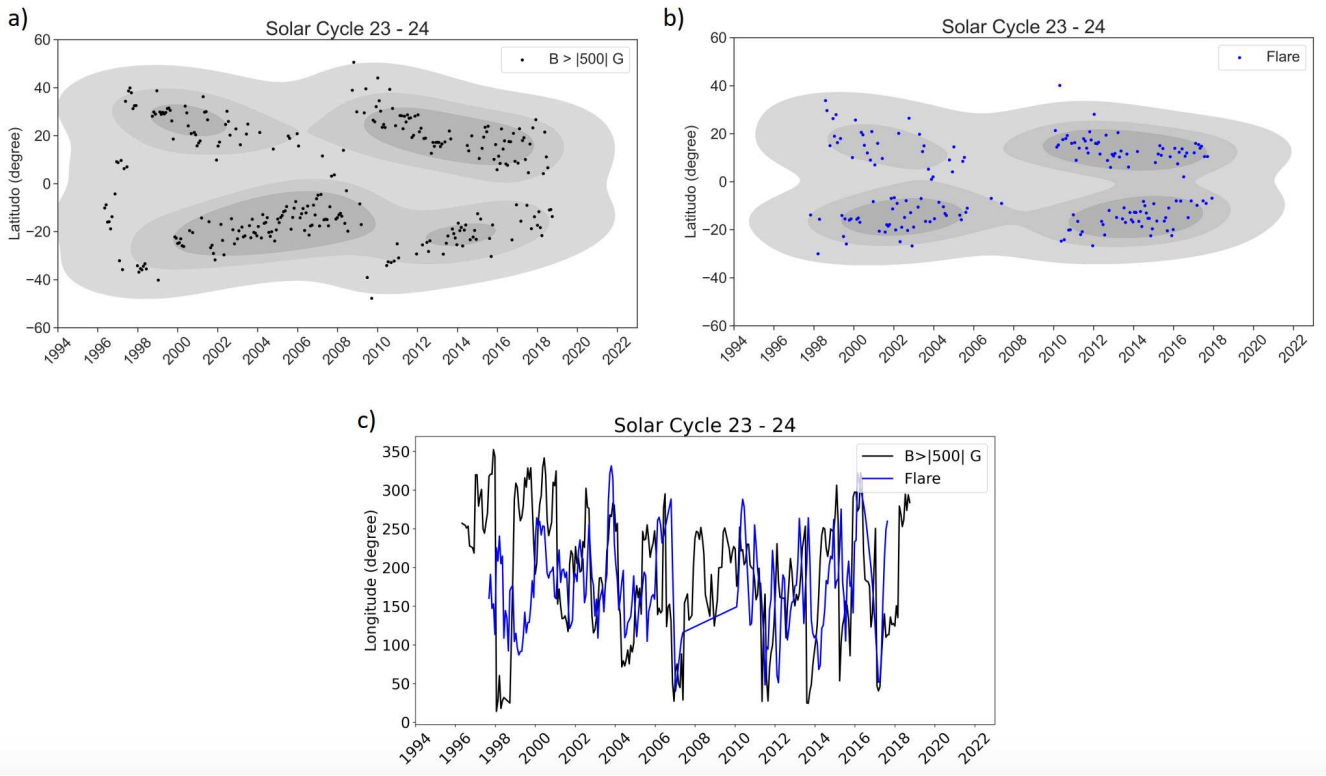

Figure 3. Panels display the most populated latitude for each CR determined by KDE in the case of (a) strong magnetic field elements and (b) flares during solar cycles (SC) 23 and 24, respectively. The gray contour plots are the results of the 2D KDE, with a smoothed color density representation of the resulting scatterplots. In panel (c), we can observe the evolution of the most populated of the strong magnetic field elements (black curves) and flares (blue curves) during SC 23 and 24.

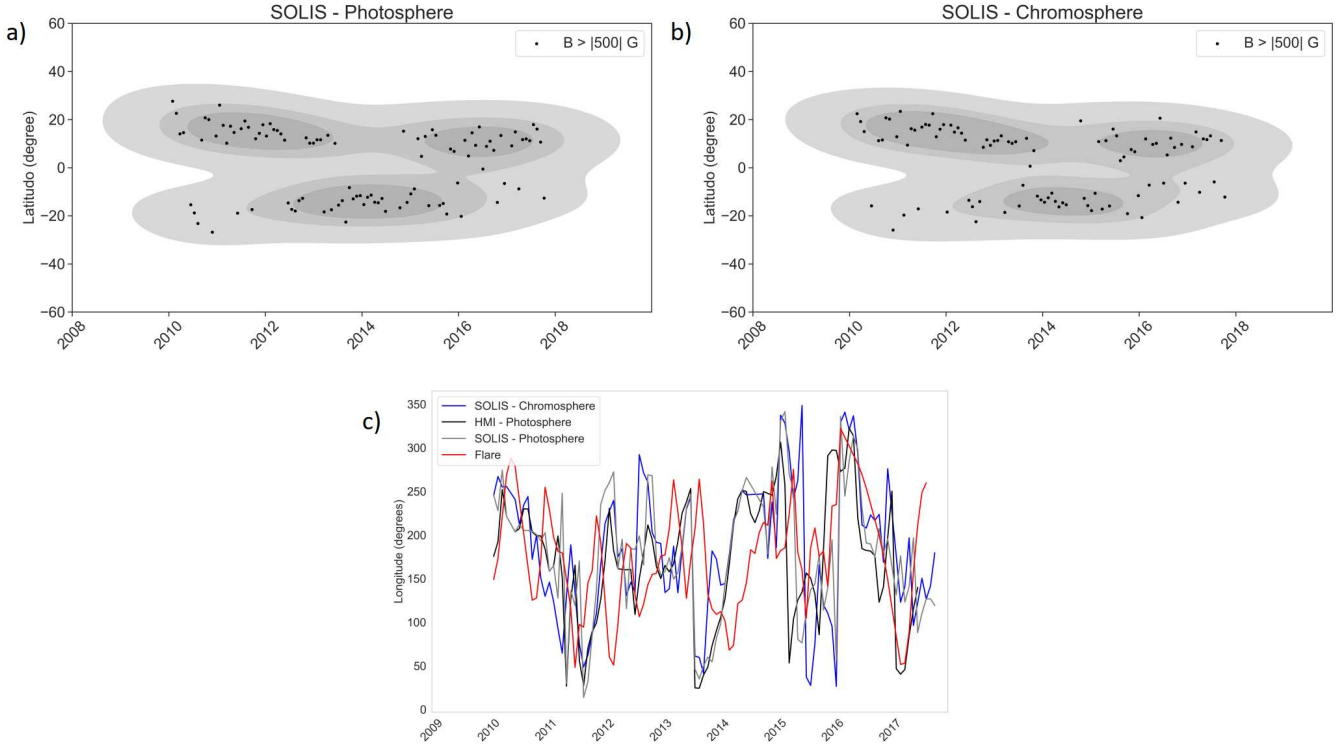

Figure 4. Panels displaying the most populated latitude for each Carrington rotation (CR) determined by KDE for strong magnetic field elements: (a) at the photosphere and (b) in the chromosphere, based on SOLIS synoptic maps during solar cycle 24. Similar to Figure 3, the gray contour plots here also represent the results of the 2D KDE. In panel (c), we can observe the evolution of the most populated longitude of strong magnetic field elements on the HMI photospheric synoptic map (black curves), the SOLIS photospheric synoptic map (gray curve), the SOLIS chromospheric synoptic map (blue curve), and flares (red curves) during solar cycle 24.

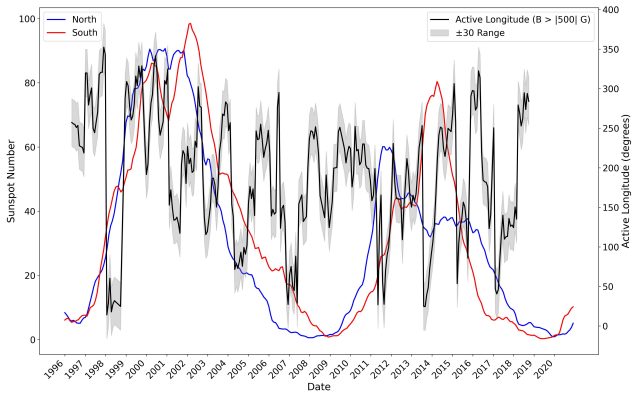

Figure 5. Figure displaying the evolution of sunspot numbers and populated longitudes from 1996 to 2020. The blue and red curves represent the monthly smoothed sunspot numbers for the northern and southern hemispheres, respectively. The black curve shows the evolution of the populated longitudes ($B > |\pm 500|$G), with the gray shaded area indicating the $\pm 30^{\circ}$ range around the populated longitude, as an active longitude can be 60° wide.

relationships between strong magnetic field elements and flare activity, but now in their longitudinal distribution.

3.3. Populated Longitudes

Therefore, as a next step, we examine the evolution of the most populated longitudinal locations, identified as the largest peaks in the KDE analysis for both strong magnetic field elements and flares across each synoptic map. These populated longitudes are shown separately for strong magnetic field elements and flares throughout solar cycles 23 and 24 in Figure 3(c), represented by black and blue lines, respectively.

We observed that the preferred longitudes for solar flares closely followed a similar trend to those of strong magnetic field elements. While some divergence between the two curves was observed during the early rising phases of the cycles, they became more closely aligned during the maximum and declining phases, as shown in Figure 3(c). We also compared, as in the latitudinal analysis, the evolution of the populated longitudes of strong magnetic field elements using SOLIS photospheric, chromospheric, and HMI synoptic maps. The populated longitudes derived from SOLIS photospheric (gray curve) and chromospheric magnetograms (blue curve) follow the same general trend as those identified in the HMI analysis (black curve), as shown in Figure 4(c). Minor discrepancies between the curves likely result from differences in the observational methods.

To better visualize the evolution of populated longitudes throughout solar cycles 23 and 24, we refer to Figure 5. This figure displays the evolution of sunspot numbers and populated longitudes from 1996 to 2020. The blue and red curves indicate the monthly smoothed sunspot numbers for the northern and southern hemispheres, respectively. The black curve traces the evolution of the populated longitudes ($B > |\pm 500|$ G), while the gray shaded region denotes the $\pm 30^{\circ}$ zone around these longitudes, reflecting the typical $\sim 60^{\circ}$ width of an active longitude. We found that, during both solar cycles, the populated longitudes persisted for four to nine CRs before shifting by approximately 160°–180°, except during the minimum period. Interestingly, during the solar minimum between solar cycles 23 and 24, the populated longitudes remained clustered around 200° Carrington longitude.

3.4. Periodicity Analysis of the Populated Longitudes

Let us now focus on the temporal (i.e., periodic) behavior of the populated longitudes of magnetic structures and the populated longitude of flares in Figures 3(c) and 4(c). To identify periodic patterns in the time series of these longitudes, wavelet analysis was performed using the method developed by C. Torrence & G. P. Compo (1998). To detect potential periodic signals, the employed wavelet power spectra was the default Morlet wavelet profile, utilizing the Python version of the C. Torrence & G. P. Compo (1998) wavelet script, available on their website.[11] The significance level of the wavelet power spectra was set at the 95% confidence level, established using a white noise model and the standard deviation of the input signal.

During solar cycle 23 (see Figure 6), the obtained periods were 0.75 yr (10 CRs) and 1.42 yr (19 CRs) in the time series of populated longitudes of strong magnetic field elements, based on the SOHO/MDI data. In the case of flares, the periods identified in their populated longitudes were 0.6 yr (8 CRs), 1.27 yr (17 CRs), and 2.02 yr (27 CRs).

During solar cycle 24 (see Figure 7), since the evolution of populated longitudes of strong magnetic field elements showed a similar pattern in both the SOLIS magnetic synoptic maps and the SDO/HMI synoptic maps, the discussion now focuses on the periods found from the SOLIS data. The identified periods are 0.67 yr (9 CRs) and 1.87 yr (25 CRs) based on photospheric data, while in the chromospheric data, the periods are 0.6 yr (8 CRs) and 1.87 yr (25 CRs). For flares, the identified periods were 0.67 yr (9 CRs) and 1.49 yr (20 CRs).

These measured periods are in good agreement with previous studies reporting periodicities in the properties of localized magnetic features over solar cycle timescales. D. A. Juckett (2006), S. Mandal et al. (2017), T. S. Kiss & R. Erdélyi (2018), N. Gyenge et al. (2016), and I. Tähtinen et al. (2024) also reported periods of approximately 0.9–2.2 yr, during which active longitudes were observed. These periods are frequently associated with the quasi-biennial oscillation (QBO) and its subharmonics, linking them to some deeper processes in the solar interior (E. V. Ivanov 2007; G. Bazilevskaya et al. 2014).

3.5. Connection between the β–γ–δ-type Active Regions and Active Longitude

For midterm solar flare prediction, it is important to investigate whether magnetically complex active regions—those most capable of producing energetic X-class flares, which are often accompanied by large coronal mass ejections—tend to appear near active longitudes.

X-class flares most commonly originate from β–γ–δ-type active regions (W. Mohamed et al. 2018), which exhibit the most complex magnetic field configurations, with umbrae of opposite polarities contained within a single penumbra. Since not all magnetically complex active regions produce X-class flares or necessarily align with active longitudes, we examined this relationship in more detail. Specifically, let us consider each active region that was classified as β–γ–δ even for a single day. The list of these active regions for solar cycles 23 and 24 was obtained from the Heliophysics Event Catalog.[12]

[11] https://atoc.colorado.edu/research/wavelets/
[12] http://helio.mssl.ucl.ac.uk/hec/hec_gui.php/

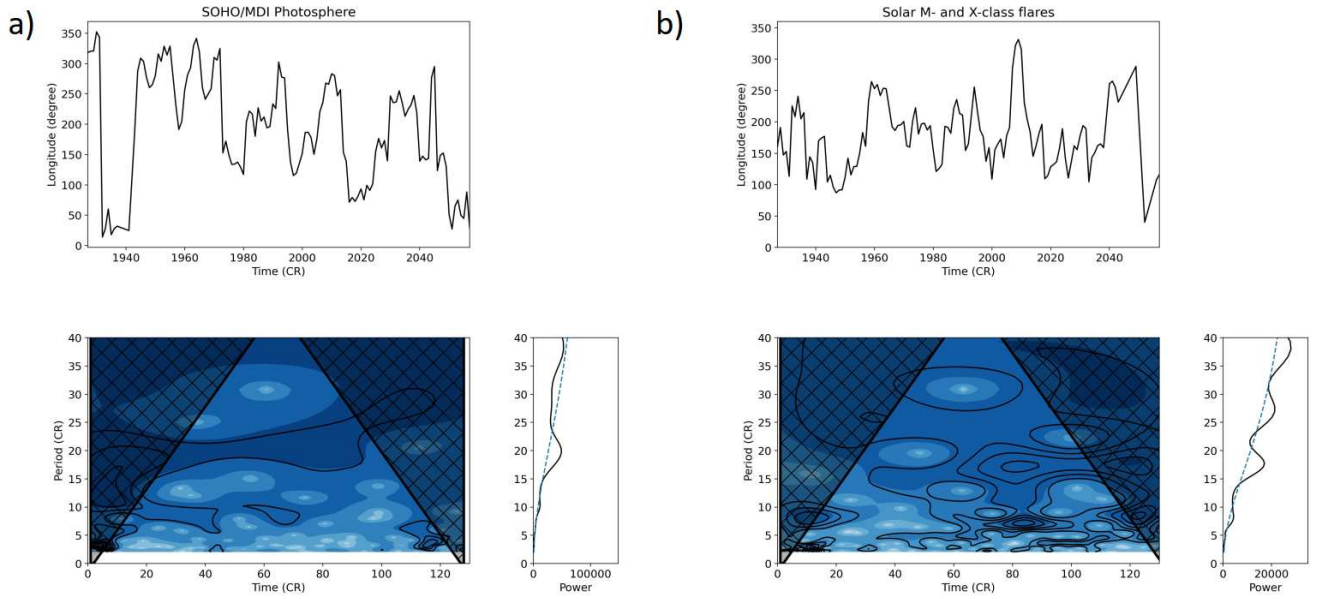

Figure 6. Wavelet figure presenting the results of the periodicity analysis of solar cycle 23 data. The upper plots in panels (a) and (b) correspond to the analysis of the active longitudes of magnetic structures and flares, respectively. The bottom left pair of panels shows the wavelet power spectra of the corresponding time series. In each wavelet power spectrum plot, the *x*-axis represents the time of the data, while the *y*-axis indicates the period in Carrington rotations. In the wavelet power spectrum plots, the hatched black lines outline the cone of influence, where edge effects may affect the results. The black contours enclose regions that exceed the 2σ confidence level for a white noise process. The right panels next to each wavelet power spectrum display the corresponding global wavelet spectra, with the power averaged over time. The blue dashed lines indicate the 2σ confidence level in these global wavelet spectra.

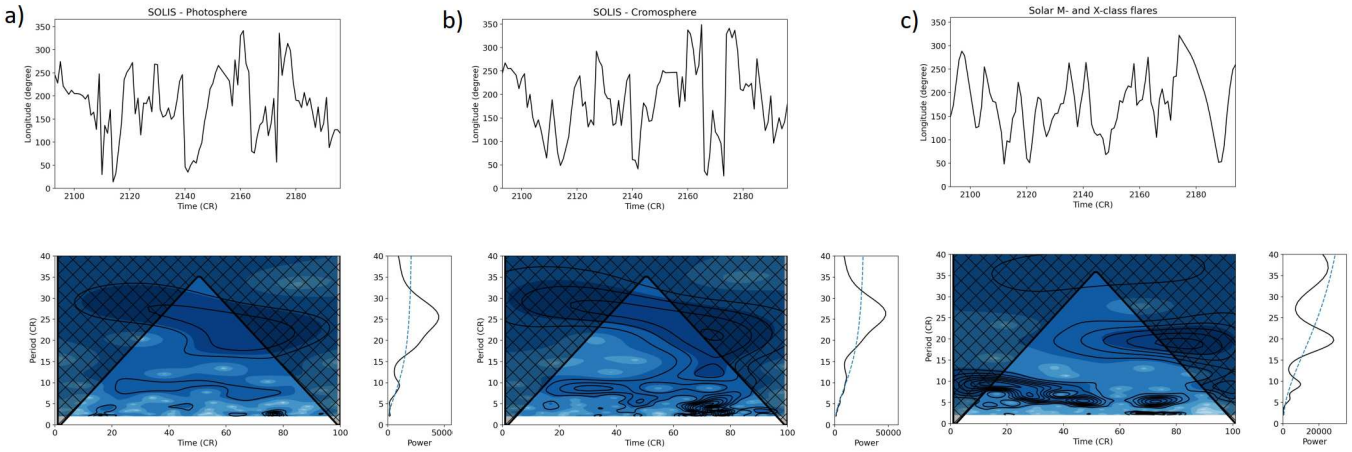

Figure 7. This figure, similar to Figure 6, presents the results of the wavelet analysis for solar cycle 24, based on SOLIS photospheric and chromospheric data, as well as flare observations.

Given that active longitudes can span approximately 60°, we considered a ±30° interval centered around the identified active longitude for each CR. We compared the Carrington longitudes of each of the 383 β–γ–δ-type active regions to determine whether they appeared close to active longitudes. Based on this analysis, we found that only 48% of the β–γ–δ-type active regions during solar cycles 23–24 appeared near active longitudes. In contrast, 71% of the β–γ–δ-type active regions that hosted X-class flares were located along active longitudes. This suggests that active longitudes may indeed be preferred locations for the most flare-productive active regions. If we can estimate the location of the active longitude, this could help us identify which β–γ–δ-type active regions have a higher probability of producing large solar eruptions. Consequently, we could focus more intensive studies on these regions, having already filtered out which active regions require greater attention compared to others.

4. Conclusion

Nevertheless, the underlying mechanisms driving the spatiotemporal patterns of active longitudes remain a topic of ongoing debate. It also remains an open question whether the concept of active longitudes can meaningfully contribute to improving the prediction of enhanced solar activity. The presented study further investigated the relationship between the most populated latitudes and longitudes of strong magnetic field concentrations and energetic flares, the distribution of magnetically complex active regions relative to active longitudes, and the positioning of regions that produced the most powerful flares in relation to active longitudes. To explore the longitudinal and latitudinal relationships between regions of

strong magnetic fields ($|B| > 500$ G) and intense flare activity during solar cycles 23 and 24, we analyzed the GOES flare database, focusing exclusively on M- and X-class flares. Synoptic magnetic maps from SOHO/MDI and SDO/HMI were used, and for solar cycle 24 (2010–2017), we additionally incorporated SOLIS radial magnetic flux synoptic maps for both the photosphere and chromosphere. The primary aim of this study was to assess whether strong magnetic field elements and high-energy flares exhibit statistically significant clustering in both longitude and latitude. To analyze these spatial patterns, we applied KDE to the distributions of strong magnetic field elements and flare locations. This approach yielded the following key findings:

1. The latitudinal distribution shows a clear north–south asymmetry during the progression of the two solar cycles. More specifically, the 2D KDE analyses revealed that solar activity was more prominent in the northern hemisphere during the rising phases of solar cycles 23 and 24, shifted to the southern hemisphere during the maximum. In the case of solar cycle 24, actually, the stronger activity returned to the northern hemisphere during the declining phase. This pattern was not observed in solar cycle 23.
2. Strong magnetic field elements and large energetic flares exhibited significant longitudinal clustering, particularly in persistent active longitudes. These longitudes remained stable over time for four to nine CRs before flipping by approximately 160°–180°, a pattern that continued through the cycle's peak and decline during solar cycles 23 and 24. The time series of active longitudes and the most populated flare longitudes show better alignment during the maximum and declining phases of the solar cycles. These activity zones are preferential sites for repeated magnetic flux emergence, rather than being sustained solely by a single large sunspot group. In fact, only a small number of active regions persist for around two CRs, with just a few—such as AR 10486 and AR 12192—surviving for three or four rotations (K. Jain et al. 2017, 2021).
3. The evolution of active longitudes also exhibits periodic behavior during both solar cycles. We observed shorter-period signals just below 1 yr, in the 0.6–0.75 yr range, as well as longer-period signals around 1.2–2 yr. For the most populated longitudes, a dominant period of approximately 1.42 yr was identified during solar cycle 23, and 1.87 yr during solar cycle 24. In the case of flare activity, the strongest periodicities were around 2.02 yr in solar cycle 23 and 1.49 yr in solar cycle 24. These measured periods are consistent with the so-called QBOs.
4. During the solar minimum between solar cycles 23 and 24, active longitudes clustered around 200° Carrington longitude for approximately 3 yr. This suggests that solar activity diminished near 200°—measured in Carrington longitude—at the end of cycle 23 and resumed roughly at the same location at the beginning of cycle 24.
5. N. Gyenge et al. (2016) suggested that flare-productive active regions tend to be located within or near the active longitudinal belt, noting that more than 60% of flares occurred within ±36° of the identified active longitude. In our analysis, we found that 71% of the β–γ–δ active regions that produced X-class flares were situated along active longitudes. This higher percentage can be attributed to the fact that we considered only M- and X-class flares, whereas L. Zhang et al. (2011), N. Gyenge et al. (2016) included all flare classes. We did not take them into account because lower-energy GOES flares occur more frequently and can appear almost anywhere on the Sun.

The presence of QBO signals in the time series of the most populated longitudes, along with the identified north–south asymmetry, supports the notion that active longitudes are strongly connected to the toroidal magnetic field in the deep convection zone. This is supported by the link between hemispheric asymmetry and QBOs (O. G. Badalyan & V. N. Obridko 2011, 2017), as well as by the proposed source region of the QBO, which lies below 0.78 $R_{\odot}$ (F. Inceoglu et al. 2007). Additionally, the identification of both longer-period (greater than 1 yr) and shorter-period (less than 1 yr) oscillations—though there is ongoing debate as to whether the latter should be classified as Rieger-type periodicities or as part of the broader QBO spectrum (G. Bazilevskaya et al. 2014, for a review)—in the evolution of active longitudes across both solar cycles supports the idea that active longitudes likely form through the amplification of localized magnetic fields. These, in turn, are shaped and intensified by convective flows, as discussed in several theoretical frameworks (M. A. Weber et al. 2023, for a review). Moreover, we found that the emergence of new cycle active regions often occurs early in the cycle within the same longitudinal intervals where active regions from the previous cycle have recently decayed, as also pointed out by V. Bumba et al. (2000). This behavior implies that active regions in a new cycle may be magnetically linked to those of the previous cycle through a shared background field structure shaped by the global dynamo.

Last but not least, our findings further support the hypothesis that active longitudes should play a crucial role in solar eruption forecasting—an idea previously mentioned by L. Zhang et al. (2011) and N. Gyenge et al. (2016), but not explored in detail as we have done here. Specifically, our results show that magnetically complex active regions responsible for major solar eruptions predominantly emerged within active longitudes. Therefore, active longitudes appear to be ideal candidates for bridging medium-term and short-term flare prediction strategies.

As a next step, we propose to evaluate whether active longitude can serve as a predictive bridge between short- and medium-term flare forecasting, by analyzing the preeruptive evolution of magnetically complex regions using proxy parameters to assess their eruption potential both within and outside active longitudes. In addition, we aim to investigate whether the QBO of active longitudes could be used to predict the longitudinal flipping to see which longitudinal zones are likely to become the next dominant active longitudes. This would allow future observational and forecasting efforts to focus increased attention on those emerging active zones.

Acknowledgments

M.B.K. is grateful for the Leverhulme Trust ECF-2023-271. M.B.K. and R.E. acknowledge the NKFIH OTKA (Hungary, grant No. K142987). R.E. is grateful to the Science and Technology Facilities Council (STFC, grant No. ST/M000826/1) UK, acknowledges PIFI (China, grant No.

2024PVA0043), and the NKFIH (Hungary) Excellence Grant (grant No. TKP2021-NKTA-64) for enabling this research.

ORCID iDs

Marianna B. Korsós https://orcid.org/0000-0002-0049-4798
Robertus Erdélyi https://orcid.org/0000-0003-3439-4127

References

Badalyan, O. G., & Obridko, V. N. 2011, NewA, 16, 357
Badalyan, O. G., & Obridko, V. N. 2017, A&A, 603, A109
Bai, T. 1988, ApJ, 328, 860
Bai, T. 1990, ApJL, 364, L17
Bai, T. 2003, ApJ, 585, 1114
Balasubramaniam, K. S., & Pevtsov, A. 2011, Proc. SPIE, 8148, 814809
Balthasar, H., & Schüssler, M. 1984, SoPh, 93, 177
Bazilevskaya, G., Broomhall, A. M., Elsworth, Y., & Nakariakov, V. M. 2014, SSRv, 186, 359
Benevolenskaya, E. E., Kosovichev, A. G., & Scherrer, P. H. 1999, SoPh, 190, 145
Berdyugina, S. V., & Järvinen, S. P. 2005, AN, 326, 283
Berdyugina, S. V., & Usoskin, I. G. 2003, A&A, 405, 1121
Bertello, L., Pevtsov, A. A., Petrie, G. J. D., & Keys, D. 2014, SoPh, 289, 2419
Bourgeois, S., Chierichini, S., Soós, S., et al. 2025, A&A, 693, A301
Bumba, V., Garcia, A., & Klvaňa, M. 2000, SoPh, 196, 403
Bumba, V., & Howard, R. 1969, SoPh, 7, 28
Canfield, R. C., & Pevtsov, A. A. 1998, in ASP Conf. Ser. 140, Synoptic Solar Physics, ed. K. S. Balasubramaniam, J. Harvey, & D. Rabin (San Francisco, CA: ASP), 131
Carrington, R. C. 1863, Observations of the Spots on the Sun: from November 9, 1853, to March 24, 1861, made at Redhill (London: Williams and Norgate)
Castenmiller, M. J. M., Zwaan, C., & van der Zalm, E. B. J. 1986, SoPh, 105, 237
Elek, A., Korsós, M., Dikpati, M., et al. 2024, ApJ, 964, 112
Gaizauskas, V., Harvey, K. L., Harvey, J. W., & Zwaan, C. 1983, ApJ, 265, 1056
Gyenge, N., Ludmány, A., & Baranyi, T. 2016, ApJ, 818, 127
Gyenge, N., Singh, T., Kiss, T. S., Srivastava, A. K., & Erdélyi, R. 2017, ApJ, 838, 18
Inceoglu, F., Howe, R., & Loto'aniu, P. T. M. 2007, ApJ, 925, 170
Ivanov, E. V. 2007, AdSpR, 40, 959
Jain, K., Lindsey, C., & Tripathy, S. C. 2006, RNAAS, 5, 253
Jain, K., Tripathy, S. C., & Hill, F. 2017, ApJ, 849, 94
Juckett, D. A. 2006, SoPh, 237, 351
Keller, C. U., Harvey, J. W., & Giampapa, M. S. 2003, Proc. SPIE, 4853, 194
Kiss, T. S., & Erdélyi, R. 2018, ApJ, 857, 113
Kiss, T. S., Gyenge, N., & Erdélyi, R. 2017, ApJ, 835, 47
Korsós, M. B., Elek, A., Zuccarello, F., & Erdélyi, R. 2024, ApJ, 975, 248
Liu, Y., Hoeksema, J. T., Sun, X., & Hayashi, K. 2017, SoPh, 292, 29
Malik, A., & Bohm, M. 2009, arXiv:0909.2973
Mandal, S., Chatterjee, S., & Banerjee, D. 2017, ApJ, 835, 62
McIntosh, S. W., Cramer, W. J., Pichardo Marcano, M., & Leamon, R. J. 2017, NatAs, 1, 0086
Mikhailutsa, V. P., & Makarova, V. V. 1994, SoPh, 155, 391
Mohamed, W., Yousef, S., & Shaltout, M. 2018, EJRSS, 21, 249
Mursula, K., & Hiltula, T. 2004, SoPh, 224, 133
Parzen, E. 1962, The Annals of Mathematical Statistics, 33, 1065
Pelt, J., Brooke, J. M., Korpi, M. J., & Tuominen, I. 2006, A&A, 460, 875
Pelt, J., Tuominen, I., & Brooke, J. 2005, A&A, 429, 1093
Pevtsov, A. A., & Balasubramaniam, K. S. 2003, AdSpR, 32, 1867
Pevtsov, A. A., & Canfield, R. C. 1999, GMS, 111, 103
Pevtsov, A. A., & Canfield, R. C. 2000, JApA, 21, 185
Rosenblatt, M. 1956, The Annals of Mathematical Statistics, 27, 832
Ruzmaikin, A., Feynman, J., Neugebauer, M., & Smith, E. J. 2001, JGR, 106, 8363
Sattarov, I., Pevtsov, A. A., Karachik, N. V., & Sattarova, B. J. 2005, in ASP Conf. Ser. 346, Large-scale Structures and their Role in Solar Activity, ed. K. Sankarasubramanian, M. Penn, & A. Pevtsov (San Francisco, CA: ASP), 395
Scherrer, P. H., Bogart, R. S., Bush, R. I., et al. 1995, The SOHO Mission (Dordrecht: Kluwer), 129
Scherrer, P. H., Schou, J., Bush, R. I., et al. 2012, SoPh, 275, 207
Schou, J., Scherrer, P. H., Bush, R. I., et al. 2012, SoPh, 275, 229
Stanek, W. 1972, SoPh, 27, 89
Tähtinen, I., Asikainen, T., & Mursula, K. 2024, A&A, 688, L32
Takalo, J., & Mursula, K. 2002, GeoRL, 29, 1317
Tian, L., Bao, S., Zhang, H., & Wang, H. 2001, A&A, 374, 294
Torrence, C., & Compo, G. P. 1998, BAMS, 79, 61
Usoskin, I. G., Berdyugina, S. V., Moss, D., & Sokoloff, D. D. 2007, AdSpR, 40, 951
Vitinskij, J. I. 1969, SoPh, 7, 210
Weber, M. A., Schunker, H., Jouve, L., & Işık, E. 2023, SSRv, 219, 63
Zhang, H., & Bao, S. 1999, ApJ, 519, 876
Zhang, L., Mursula, K., Usoskin, I., & Wang, H. 2011, A&A, 529, A23
Zhang, L. Y., Wang, H. N., Du, Z. L., Cui, Y. M., & He, H. 2007, A&A, 471, 711